arXiv:2009.07157v2 [cond-mat.str-el] 24 Feb 2022

Multiple mobile excitons manifested as sidebands in quasi-one-dimensional metallic $TaSe_3$

J.-Z. Ma,[1,2,3,*] S.-M. Nie,[4] X. Gui,[5] M. Naamneh,[2] J. Jandke,[2] C. Y. Xi,[6] J. L. Zhang,[6] T. Shang,[7] Y. M. Xiong,[6] I. Kapon,[8] N. Kumar,[9] Y. Soh,[9] D. Gosalbez-Martinez,[10] O. Yazyev,[10] W. H. Fan,[11,12] H. Hubener,[13] U. De Giovannini,[13] N. C. Plumb,[2] M. Radovic,[2] M. A. Sentef,[13] W.-W. Xie,[14] Z. Wang,[11,12] Christopher Mudry,[15,10] M. Müller,[15,*] and M. Shi[2,*]

[1] *Department of Physics, City University of Hong Kong, Kowloon, Hong Kong, China*

[2] *Swiss Light Source, Paul Scherrer Institute, CH-5232 Villigen PSI, Switzerland*

[3] *City University of Hong Kong Shenzhen Research Institute, Shenzhen, China*

[4] *Department of Materials Science and Engineering, Stanford University, Stanford, CA 94305, USA*

[5] *Department of Chemistry, Princeton University, Princeton, New Jersey 08540, USA*

[6] *Anhui Province Key Laboratory of Condensed Matter Physics at Extreme Conditions, High Magnetic Field Laboratory, Chinese Academy of Sciences, Hefei, Anhui 230031, China*

[7] *Key Laboratory of Polar Materials and Devices (MOE), School of Physics and Electronic Science, East China Normal University, Shanghai 200241, China*

[8] *Department of Quantum Matter Physics, University of Geneva, 24 Quai Ernest-Ansermet, 1211 Geneva, Switzerland*

[9] *Paul Scherrer Institute, CH-5232 Villigen PSI, Switzerland*

[10] *Institute of Physics, École Polytechnique Fédérale de Lausanne (EPFL), CH-1015 Lausanne, Switzerland*

[11] *Beijing National Laboratory for Condensed Matter Physics and Institute of Physics, Chinese Academy of Sciences, Beijing 100190, China*

[12] *University of Chinese Academy of Sciences, Beijing 100049, China*

[13] *Max Planck Institute for the Structure and Dynamics of Matter, 22761 Hamburg, Germany*

[14] *Department of Chemistry and Chemical Biology, Rutgers University, Piscataway, New Jersey 08854, USA*

[15] *Condensed Matter Theory Group,*
Paul Scherrer Institute, CH-5232 Villigen PSI, Switzerland

Abstract

Charge neutrality and an expected itinerant nature makes excitons potential transmitters of information. However, exciton mobility remains inaccessible to traditional optical experiments that only create and detect excitons with negligible momentum. Here, using angle-resolved photoemission spectroscopy, we detect dispersing excitons in quasi-one-dimensional metallic trichalcogenide, $TaSe_3$. The low density of conduction electrons and low dimensionality in $TaSe_3$ combined with a polaronic renormalization of the conduction band and the poorly screened interaction between these polarons and photo-induced valence holes leads to various excitonic bound states that we interpret as intrachain and interchain excitons, and possibly trions. The thresholds for the formation of a photohole together with an exciton appear as side valence bands with dispersions nearly parallel to the main valence band, but shifted to *lower* excitation energies. Interestingly, the energy separation between side and main valence band can be controlled by surface doping, enabling the tuning of certain exciton properties.

* Corresponding authors:

junzhama@cityu.edu.hk, markus.mueller@psi.ch, ming.shi@psi.ch

Introduction Low-dimensional electronic systems with a low density of charge carriers n_c exhibit interesting many-body effects. Indeed, their Fermi energy is low as compared to the strength of the Coulomb interaction, which is poorly screened. Moreover, the low dimensionality enhances interaction effects. They manifest themselves in non-Fermi liquid gapless ground states such as metallic Luttinger liquids or gapped ground states such as insulating Wigner crystals and other kinds of charge density waves [1, 2]. Not only the ground state of such strongly interacting systems, but also their excitations exhibit interesting strong coupling phenomena. In particular, the attraction between negatively charged electrons and positively charged holes can lead to bound states in the excitation spectrum, usually referred to as excitons [3–8], and this tendency is enhanced in low dimensions.

The creation in insulators of *non-moving* excitons [that is, bound states from electrons and holes located at the minimum and maximum of the conduction band (CB) and valence band (VB), respectively] by optical excitation is fairly standard [5, 6, 8]. Very recently, distinct branches of *dispersing* excitons have been observed in free-standing monolayer WSe_2, a two-dimensional Dirac band insulator, by momentum-resolved electron energy-loss spectroscopy [9]. However, the observation of mobile bound states with sharp dispersions in *metals* has remained elusive for various reasons. Higher-dimensional metals are unlikely to host excitons. First, their creation requires an exceedingly strong (despite screening) Coulomb interaction that is not preempted by an interaction-driven instability to an insulator. Second, the excitation of moving excitons with light involves higher-order processes, whose cross-sections are very weak, unless low dimensionality and low carrier density (as present in $TaSe_3$) allow for strong Coulomb interactions with small momentum transfer. The heavy quasiparticles (polarons) constitute a third favorable attribute of $TaSe_3$, as their mass increases the binding energy of the resulting excitons (see Supplemental Material for a more detailed discussion).

The interplay of dilute conduction electrons, low effective dimensionality, and heavy quasiparticles in $TaSe_3$ makes this Q1D material a prime candidate for probes of excitonic effects by ARPES.

We have systematically studied the metallic phase of $TaSe_3$ using ARPES and observed the following features at low temperature. (1) Several side-valence bands (SVBs) appear *exclusively above* a pronounced VB – in contrast to most ARPES spectra that report sidebands (Figs. S1-S3 of the Supplementary Material). (2) Their dispersions are roughly parallel to the VB. (3) When the surface carrier density is increased by doping, the energy separations

between the SVBs increase. (4) Close to the Fermi level, the CB is heavily renormalized, and the coherent quasiparticle peak follows a W-shaped dispersion. As we will argue, observations (1-4) suggest that the SVBs result from strong coupling between the valence and conduction electrons and involve *mobile* bound states (excitons, and perhaps trions) that have not been observed so far using ARPES. Up to now, ARPES has detected excitonic physics only though the effects of excitonic condensation, as seen for example, in the electronic structure of Ta_2NiSe_5 near the Fermi level [10], or through the band folding due to a finite momentum condensate, for example, in 1T $TiSe_2$ [11].

Results

Material characterization The trichalcogenide $TaSe_3$ consists of covalently bonded layers, stacked and held together by weaker van der Waals forces along the direction $(10\bar{1})$ [12, 13]. Each layer consists of chains oriented along the b-axis, see Figs. 1**a-b**, with strongly anisotropic electric and optical response. The natural cleavage plane is the $(10\bar{1})$ surface. The corresponding bulk Brillouin zone (BBZ) and the $(10\bar{1})$ surface Brillouin zone (SBZ) are shown in Fig. 1**c**. In the SBZ, (k_x, k_y) denote the components of momentum along (101) and (010), respectively.

$TaSe_3$ is so far the only known trichalcogenide that is a metal at high temperature and becomes superconducting below 2K without forming a charge density wave (CDW) [14–20]. However, it is close to such a transition, as suggested by CDW-like signatures observed upon doping with Cu [21, 22], application of strain, Ref. [23] and our own surface doping results reported below. We note that topological surface states [24] have been observed in Refs. 25 and 26 in the gap between the top of the VB and the bottom of the CB of $TaSe_3$, where band inversion occurs. However, as we will argue, they are clearly distinct from the excitonic features we focus on here.

Overall band structure from ARPES We have studied the electronic structure of $TaSe_3$ with ARPES on the *in situ* cleaved surface $(10\bar{1})$. The intersection of the small three-dimensional (3D) Fermi surface (FS) with a plane spanned by momenta conjugate to the crystalline directions b and $a+c$ is seen as the region of highest intensity in Fig. 1**d**. Figure 1**e** (Γ-Y cut) shows hole-like VBs with maxima at the zone center Γ, dispersing from 0.1 eV to 2 eV. Figure 1**f** (X-S cut) shows an electron-like CB with minimum at the mid-point X on one zone edge of the BBZ. The strong anisotropy in the ac plane results in a FS in the form of an elongated elliptical electron pocket centered at X, see Fig. 1**d**, the minor axis along

the X-S direction reflecting the strong dispersion along the b-axis. There is no good nesting wave vector for the FS of $TaSe_3$ shown in Fig. 1**d**. This might rationalize the absence of a CDW phase in pristine $TaSe_3$. The coupling between stacked layers is weak. This is seen both by the elongated FS in a cut with the plane $k_x = 0$, Fig. 1**g** (the photon energy $h\nu$ being used to explore momenta normal to the cleavage plane), as well as in the similarity of the spectra in Figs. 1**h-j**, corresponding to different normal momenta. Nevertheless, Fig. 1**k** shows a definite, if small, dependence on the incoming photon energy, which we take as evidence for these bands being bulk as opposed to surface bands.

Side-valence bands (SVBs) Here, we focus our attention on SVBs, which are remarkable spectral features visible in the energy distribution curves (EDC) of the ARPES spectra. We show in Fig. 2**a** the band structure of $TaSe_3$ along the X-S direction in the BBZ predicted by density functional theory (DFT), as explained in the Methods section. There is one CB (green), lying above five VBs. The VB closest to the CB (purple) is referred to as the main-valence band (MVB). The lower lying VBs are colored in blue. These DFT bands match the five bands measured in Fig. 2**b**. The EDC along the vertical green line with fixed $k_y \approx 0.2\,\text{Å}^{-1}$ in Fig. 2**b** is shown in the boxed inset. The arrows indicate local maxima of this EDC. They move as k_y varies, defining SVB dispersions. The SVBs are bounded from below by the MVB which is stronger in intensity. The MVB and the SVBs become better visible in the curvature intensity plot of Fig. 2**c** associated with the data of Fig. 2**b**, (the color scale being related to the curvature of the ARPES intensity). For reference, Fig. 2**d** shows a schematic of the band dispersion in Fig. 2**c**. The dispersions of the MVB (purple arrow) and three SVBs (tilted red arrows) are approximately symmetric about X. The Supplementary Material shows more EDCs (Figs. S4-S7) illustrating how the SVBs are identified and evolve with doping. We only observe sidebands of the MVB, but none associated with the CB, or the deeper VBs. Close to the X point, there is no observable intensity that could be clearly assigned to either SVBs or to the MVB. In Fig. 2**d** the evolution of the MVB away from large momenta (where its peak is well resolved) is indicated by a dashed segment, delineating the "nose" predicted by DFT. We also indicate the possible continuation of SVBs as they approach the spectral features associated to the CB, colored in green in both Fig. 2**c** and Fig. 2**d**. The latter are of a polaronic origin and play an important role for the excitonic features seen in ARPES.

Polaron band In typical members of the family XT_3, such as $NbSe_3$ [18], FS nest-

ing induces a CDW instability at fairly high temperatures, pointing toward a substantial electron-phonon coupling in these materials.

In pristine $TaSe_3$, the conduction electrons give rise to two branches of excitations, as traced by the maxima of the EDCs in Figs. 2**e** and 2**f**. The branch of "bare" electron excitations yields a parabolic CB with a fairly short life time, showing up as a broad hump as a function of energy. Much sharper, phonon-dressed quasiparticle (QP) excitations form a strongly renormalized, weakly dispersive polaron branch close to the Fermi energy, separated by a dip from the hump of bare excitations. The spectral weight of the heavy polaron band is strongest close to k_{F} and becomes very weak for $k_y \approx 0$. Furthermore the dispersion of the maximal spectral weight is not essentially flat as expected for a simple heavy polaron, but follows a non-monotonic W shape, see Fig. 2**g**. Such a dispersion might arise due to the hybridization of the polaron band with a dispersing composite excitation consisting, e.g., of a conduction electron and a nearly soft phonon. We do not explore these features in more detail here, but simply observe that they entail that the heavy polaron band effectively breaks up into two small islands concentrated just below the Fermi points $\pm k_{\mathrm{F}}$. This is important in the context of exciton formation and SVBs in ARPES.

Effects of surface doping Crucial insight into the nature of the SVBs is gained by increasing the density of surface electrons. This is achieved by evaporating potassium (K) in situ on the cleaved surface of $TaSe_3$. Here we focus on moderate doping (evaporation times of one minute or less), while stronger doping data (up to five minutes of evaporation) are reported in Fig. S9 of the Supplementary Material.

Figures 3**a** and 3**b** show the ARPES intensity after evaporation for t1 $\equiv$ 1 minute, for the same range of momenta and energies as in Fig. 2**b**. The evaporated atoms chemically dope electrons onto the surface which increases the filling of the conduction band. The incoming photons in Fig. 3**a** are circularly polarized with positive helicity, while they linearly polarized in the incident plane in Fig. 3**b** (the scattering geometry is reported in Fig. S8). EDCs, such as shown in Fig. 3**c** (or Fig. S7), allow to locate the MVB and the SVBs. More EDCs for the same evaporation time t1 can be found in Figs. S5 and S6 of the Supplementary Material. The curvature intensity plot in Fig. 3**d** shows that the two SVBs (indicated by the red arrows) are more pronounced than in the undoped case of Fig. 2**c**. A heavy, but non-monotonically dispersing polaron band close to the Fermi energy is still present, but the size of the high intensity islands of diameter Δk within the polaron band increases together with

k_F, as is apparent in Figs. 3**d**. The measured dispersions are traced in Fig. 3**e**. Note that the non-renormalized CB branch is essentially parabolic, apart from the polaronic effects close to the Fermi energy and the avoided level crossings with some SVBs, where the ARPES intensity is suppressed. For large enough momenta one identifies two SVBs roughly parallel to the MVB. At small momenta close to X, there are two nose-like dispersing pieces of an excitation branch. They might be continuations of the SVB's seen at larger momenta, as hinted in Fig. 3**f**.

Figure 3**g** shows the ARPES intensity at $h\nu = 37\,\mathrm{eV}$ after doping. Here, the first SVB is clearly visible.

The doping strongly affects the average energy separations Δ_1 and Δ_2 between the MVB and the first SVB, and the first and second SVBs (if detectable), respectively. We measure these spacings in the regime of large momenta relative to X. In Fig. 3**h**, Δ_1 and Δ_2 are seen to substantially increase with doping or, equivalently, with the Fermi wavevector k_F. In particular, $\Delta_1 \sim 180\,\mathrm{meV}$ and $\Delta_2 \sim 70\,\mathrm{meV}$, in the presence of potassium doping (t1) are much larger than the spacings $\Delta_1 \sim 70\,\mathrm{meV}$ and $\Delta_2 \sim 37\,\mathrm{meV}$ in undoped $TaSe_3$.

Effects of stronger doping are presented in Figs. S9-S10 of the Supplementary Material. The QP-dip-hump features at the Fermi energy described above evolve into a CDW at t2 $\equiv 2\,$minutes. This observation supports the interpretation of these polarons as originating from an electron-phonon coupling in $TaSe_3$. More emperical evidences for electron-phonon coupling in $TaSe_3$ is provided by the evolution of Raman intensities in Fig. S12 of the Supplementary Material.

Doping increasingly separates the QP-dip-hump features at the Fermi energy from the region of band inversion between the bottom of the CB and the top of the MVB, confirming that they are distinct, mutually independent characteristics. In particular SVBs are clearly distinct from topological surface states. The doping dependence of the ARPES spectra also rules out an interpretation of the SVBs in terms of states bound to a surface layer detached from the bulk (see Supplementary Material for further discussion).

Finally, doping reveals that, while CB and MVB are shifted by roughly the same energy at t1 $\equiv 1\,$minutes, their shift differs from the nearly rigid energy shift of the lower VBs. This suggests that the lower VBs are nearly uncorrelated with the carriers at the Fermi level, while MVB and CB are more strongly correlated with new doped carriers. This may be the reason why we observe excitons only associated with the MVB, but not with the

other VBs, (see Sec. IIIof the Supplementary Material).

Interpretation of SVBs As is explained in the Supplementary Material and summarized in Fig. 4, the position, shape, and doping dependence of the SVBs can best be explained in terms of a moving bound state between the photo-hole with non-zero group velocity and large momentum in the VB of a given chain and one (or possibly several) QPs in the CB on the same or on neighboring chains, see Figs. 4**a-b**. In particular, for sufficiently large total momentum K along the chain (as compared to Δk, the diameter of the polaronic islands), we propose the following interpretation. The MVB arises from the excitation of a single photo-hole in the VB, see Fig. 4**cI**. The top-most SVB above the MVB is the K-dependent threshold to a continuum consisting of an exciton and a free quasihole in the CB, the exciton being a moving bound state between a QP in the CB and a valence hole on the same chain, sharing the same group velocity Fig. 4**cII**. The SVBs closer to the MVB can be of two distinct origins. One possibility is that the particle-hole excitation in the CB is created on a chain neighboring the one hosting the valence hole, leading to an interchain exciton Fig. 4**cIII**, with lower binding energy than intrachain excitons. Alternatively, one can have thresholds to more complex continua, the simplest one consisting in a photo-hole accompanied by two particle-hole excitations on neighboring chains Fig. 4**cIV**, whereby both quasiparticles bind to the valence hole to form a mobile trion [27–29]. These trions are distinct from two-particle bound states (excitons) that are dressed with particle-hole excitations of the Fermi sea, occuring in optical low-momentum excitations of monolayer transition-metal dichalcogenides at finite carrier densities in Ref. 30. A trion threshold is expected to have a lower energy-integrated intensity, as it scales with a higher power of the density of conduction electrons (since it involves two particle-hole excitations), an aspect that might rationalize the low intensity of the second SVB in Fig. 3**c-d**.

The separation of the SVBs from the MVB results from two sources, the binding energy and the kinetic energy gain from distributing the momentum between the VB and the CB. We show with Fig. 4**b** how these two effects combine to produce SVBs above the MVB. The binding energy is relatively strong due to the heavy mass of the polaronic quasiparticles and the effective one-dimensionality (which entails an increase of binding energy with doping), as we discuss in Secs. VI-VIII in the Supplementary Material. In a pristine sample we estimate it to be of the order of 150 meV for the most strongly bound exciton

While the polaronic reconstruction of quasiparticles makes the formation of excitons more

robust, excitonic excitations can also occur without polaronic reconstruction, provided the Fermi surface is sufficiently small.

Discussion

The material $TaSe_3$ is a Q1D metal which combines a low density of conduction electrons with a polaronic renormalization of the low-energy quasiparticles. All these ingredients enhance the spectral weight in photoemission for composite excitations involving an exciton and a hole from the CB. Our experiments show that the excitons come with different internal structure, presumably depending on whether the involved holes and electrons belong to the same chain or neighboring ones, or whether the hole binds one or two conduction electrons (resulting in an exciton or a trion, respectively).

Interchain excitons are quasi-1D cousins of bilayer excitons in layered 2D materials, such as transition metal dichalcogenides [31, 32]. They are of particular interest as they may have a significantly longer life time than intra-chain excitons due to the spatial separation of the particle and the hole.

We have experimentally probed the evolution of these SVBs with increasing doping. The latter increases both the binding energy (owing to the Q1D nature of the problem) and the typical momentum transfer in the CB. Both increase the energy separation between the SVBs and the MVB. A more systematic study of the doping dependence will allow to analyze the fate and nature of excitons as one crosses the Lifshitz transition where a second CB emerges at the Fermi level. It would also be interesting to excite the exciton bound states at low momenta by optical absorption, or by using resonant inelastic X-ray scattering, or exciting them by means different from light. Finally, it would be interesting to see whether dispersing excitons also exist in other trichalcogenides, at least in the regime of higher temperatures where they do not form a charge density wave. This will elucidate to what extent the peculiar structure of the polaronic band with its strong intensity islands is crucial for the visibility of exciton branches in ARPES.

Acknowledgments We acknowledge E. Rienks, H. Li, Y. Hu, and V. Strokov for help during the ARPES experiments. We thank Prof. Dirk van der Marel for discussions. M.S., J.Z.M. and J.J. were supported by the Sino-Swiss Science and Technology Cooperation (Grant No. IZLCZ2-170075). M.S. was supported by the Swiss National Science Foundation under Grant No. 200021_188413. M.S., O.Y. and D.G. were supported by the NCCR MARVEL funded by the Swiss National Science Foundation. M.M. was supported by the Swiss

National Science Foundation under Grant No. 200021_166271. M.N. has received funding from the European Union's Horizon 2020 research and innovation programme under the Marie Sklodowska-Curie grant agreement No. 701647, and Swiss National Science Foundation under Grant 200021_159678. J.Z.M. was supported by City University of Hong Kong through the start-up project (Project No. 9610489), the National Natural Science Foundation of China (12104379), and Shenzhen Research Institute, City University of Hong Kong. M.A.S. is supported by Deutsche Forschungsgemeinschaft through the Emmy-Noether programme is gratefully acknowledged (SE 2558/2-1). W.W.X. was supported by Beckman Young Investigator Program funded by Arnold and Mabel Beckman Foundation and US NSF DMR-1944965. X.G. was supported by the US Department of Energy Division of Basic Energy Sciences (DG-FG02-98ER45706).

Author contributions: J.Z.M. performed ARPES experiments with the help of M.N., J.J. and W.H.F.; S.M.N. and Z.W. performed first-principles calculations of the band structure. J.Z.M. plotted all the figures. X.G. and W.W.X. synthesised the single crystals. C.Y.X. performed primary high magnetic field quantum oscillation (QO) measurements with the help of J.Z.M., J.L.Z., T.S. and Y.M.X.; H.H. and U.D.G. analyzed the possibility of boson driven band structures with the help of D.G. and O.Y.; I.K. performed Raman measurements for checking the phonon energy. N.K. and Y.S. performed primary transport measurements with PPMS; M.A.S. helped ruling out the bosonic strong coupling scenario. C.M. and M.M. analyzed different physical scenarios based on bound states and worked out the theory of excitonic side-bands. All authors contributed to the discussion of this project. J.Z.M., C.M., M.M., and M.S. wrote the manuscript.

Competing interests: The authors declare that they have no competing interests.

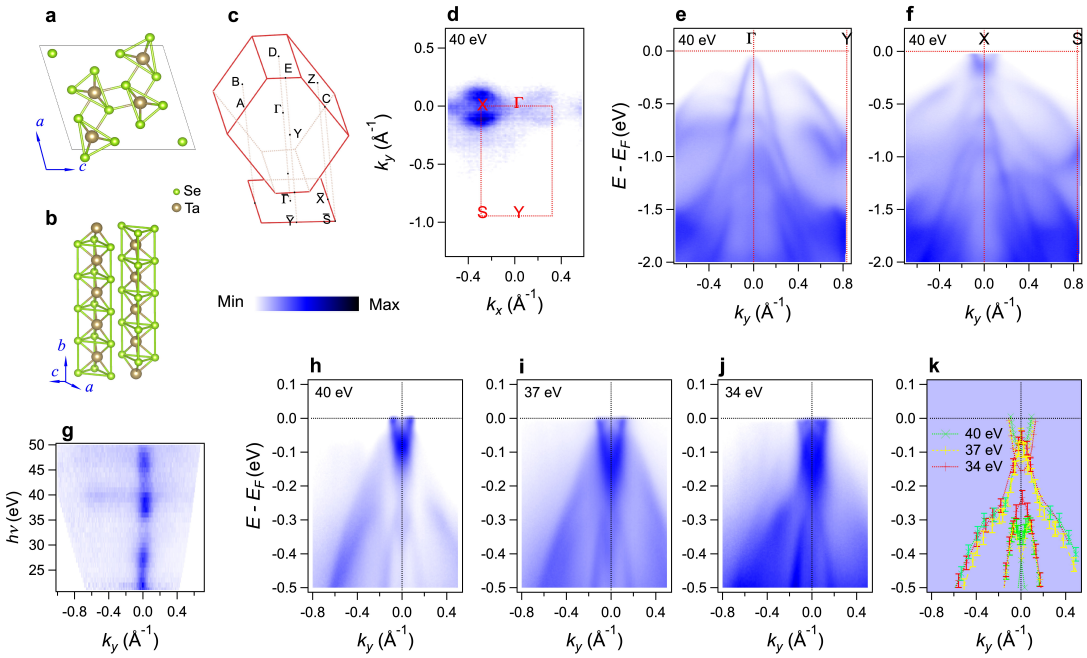


FIG. 1. The crystalline and electronic structures of $TaSe_3$ at 15K. **a** Crystal structure projected onto the a-c plane. The crystallographic axis are a, b, and c. **b** Crystal structure with its 1D chains oriented along the b axis. **c** The bulk Brillouin zone BBZ and the 2D surface Brillouin zone SBZ of the cleavage surface [normal to $(10\bar{1})$]. **d** ARPES intensity at the Fermi energy E_F as a function of the momentum $\boldsymbol{k} \in$ SBZ for incoming photon energy $h\nu = 40\,\mathrm{eV}$. The momenta k_x and k_y are conjugate to the (101) and the (010) direction, respectively. **e-f** ARPES intensities at $h\nu = 40\,\mathrm{eV}$ as a function of the energy $E - E_\mathrm{F}$ and the momentum component k_y in the SBZ, along the cut Γ-Y ($k_x = 0$) in **e**, and along the cut X-S in **f**. **g** ARPES intensity as a function of the momentum k_y and of the incoming photon energy $h\nu$, which tunes the momentum $k_\perp$ perpendicular to the planes. The intensity contour is seen to be very elongated along $k_\perp$, suggesting that the equal energy contour near Fermi level is essentially an elliptical cylinder with axis parallel to $k_\perp$. **h-j** ARPES intensities as a function of the energy $E - E_\mathrm{F}$ and the momentum k_y along the cut X-S in the SBZ for photon energies $h\nu = 40\,\mathrm{eV}$ **h**, $h\nu = 37\,\mathrm{eV}$ (i), and $h\nu = 34\,\mathrm{eV}$ **j**. **k** Superimposed band dispersions from panels **h-j** (shown there as colored continuous lines as guide to the eye). The variation with $h\nu$ implies a finite dispersion along $k_\perp$.

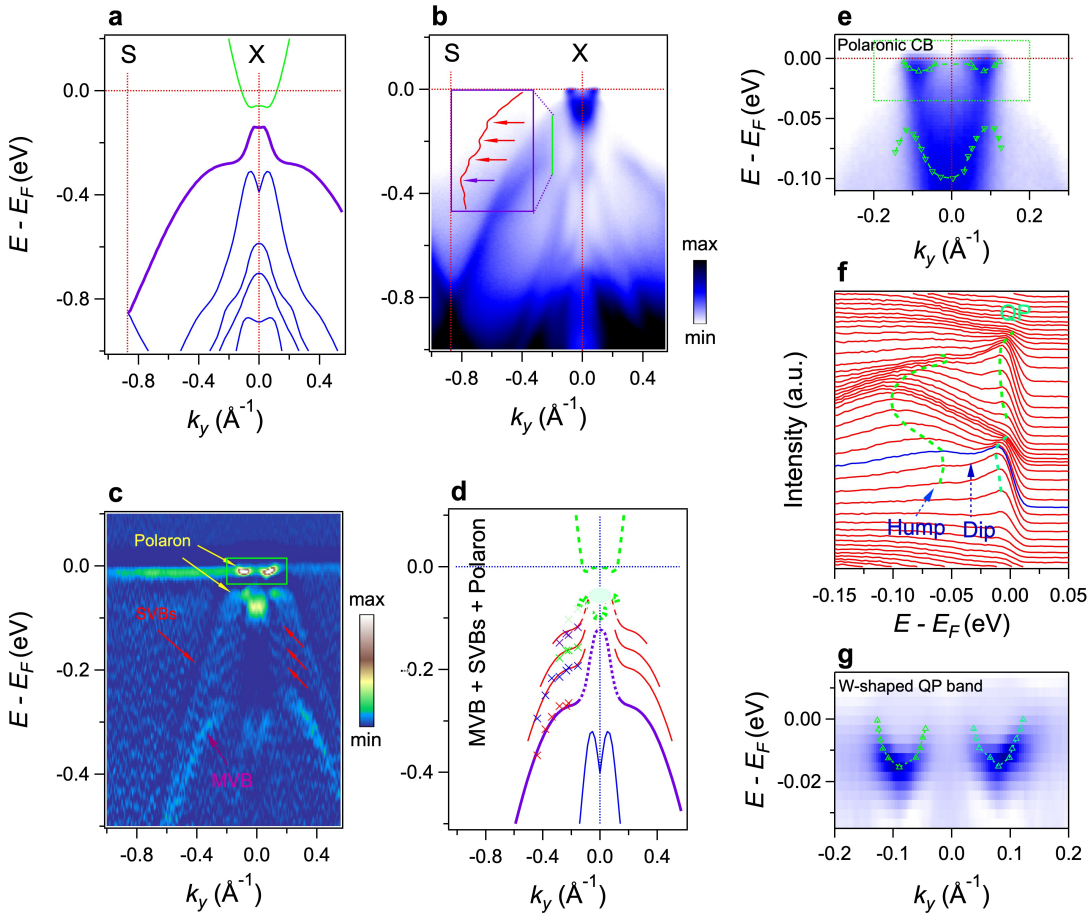


FIG. 2. Side valence bands and polarons in pristine sample. **a** Dispersion of the noninteracting (Bloch) bands of $TaSe_3$ computed using DFT (see method part). The purple band is the topmost VB, which we refer to as the MVB. It lies between one CB (colored in green) and four lower lying valence bands (colored in blue). The dispersion of all bands is symmetric about X along the X-S cut. **b** ARPES data from Fig. 1**f** with higher energy resolution and statistics. The curve in the inset shows the EDC along the green line ($k_y = -0.2\,\text{Å}^{-1}$). The red arrows point to side peaks. Their dispersions with momentum define "side valence bands" (SVBs). **c** The curvature intensity plot corresponding to the data in **b** enhances the visibility of SVBs marked by red arrows above the MVB. The green box encloses the coherent branch of the polaron quasiparticles (QPs) making up the bottom of the CB and whose spectral weight is concentrated in two small islands of diameter Δk. The broad hump indicated by a yellow arrow is the remnant of the CB that would be left, were there no interaction with a bosonic mode. **d** Schematic interpretation of the signatures seen in **c**. **e-f** Close up of the data of Fig. 1**b**. The upper and lower dashed lines in **e** trace the dispersions of the polaron QP peak and the broad hump, respectively, as visible in the EDCs in **f**. **g** Detailed view of the ARPES intensity within the polaron band of in the green box of **c**. The dashed green line indicates the extrapolated dispersion of the W-shaped QP band.

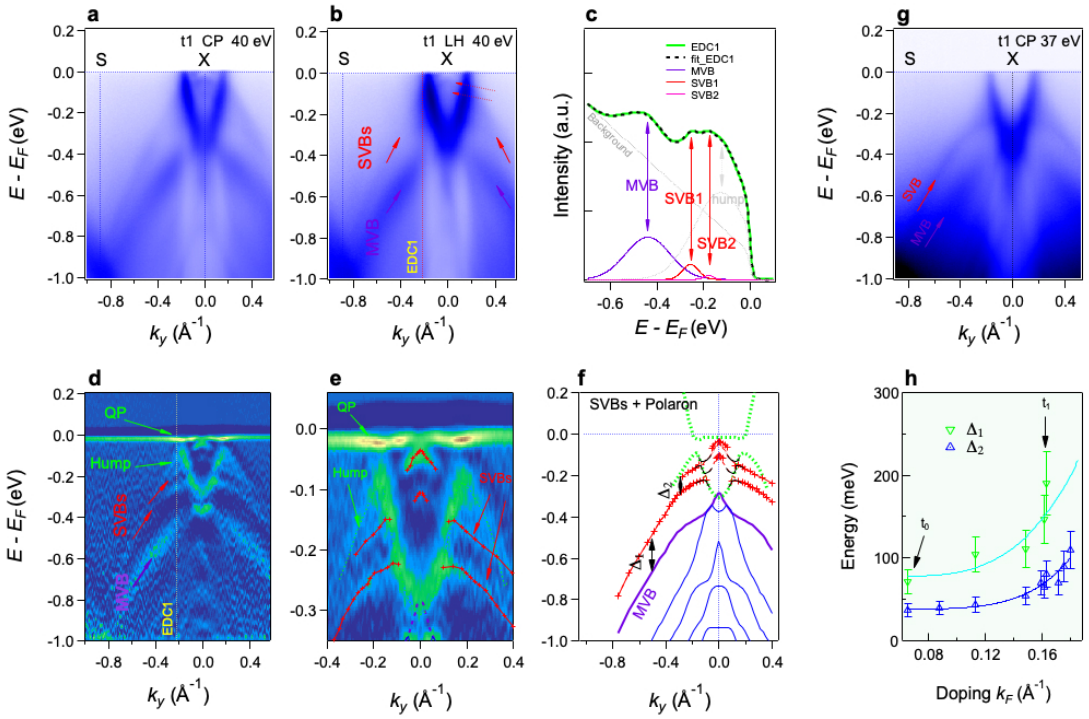


FIG. 3. Dependence on potassium doping of the electronic structure of $TaSe_3$. **a-b** ARPES intensity plot with energy measured relative to E_F and momenta along the X-S cut, after potassium was deposited for t1=1 minute on the surface of $TaSe_3$. The incoming photons are circular positive-helicity [CP,**a**] and linearly horizontal [LH, **b**] polarized, respectively. The full red arrows in **b** indicate a side valence band (SVB) above the main valence band (MVB), to which the purple arrow points. The dashed red arrows indicate additional spectral side-features at small k_y, also seen in **a**. **c** Fit of the EDC1 in panel **b**: MVB, SVB1, SVB2, and hump are modeled as Gaussians, superposed on a linear background, and cut off by the Fermi-Dirac function. Two side peaks, a strong one (SVB1) and weak one (SVB2), are visible at that value of $k_y = -0.2\,\text{Å}^{-1}$. **d** The curvature intensity plot of the ARPES intensity in **b**. The two SVBs are indicated by red arrows. The MVB peak is indicated by a purple arrow. The coherent polaron peak (QP) and the bare CB excitation (hump) are indicated by green arrows. **e** The close up of the curvature intensity plot in **d** identifies the SVBs more clearly. The red lines show the two SVB dispersions extracted from the peak positions in the curvature intensity plot. Additionally we delineate nose-like side spectral features at small k_y. **f** The band dispersions extracted from tracing the peak positions of the full spectrum in **d**. The green dotted lines are the polaronic CB and the dispersing hump of the bare CB excitation. The red lines at small $k_y \approx 0$ are sidepeaks whose vertical shift relative to the SVBs at large momenta is similar as that of the "nose"-like peak predicted by the DFT calculations of Fig. 2**a** with respect to the MVB dispersion at large k_y. The dotted red lines suggest that these

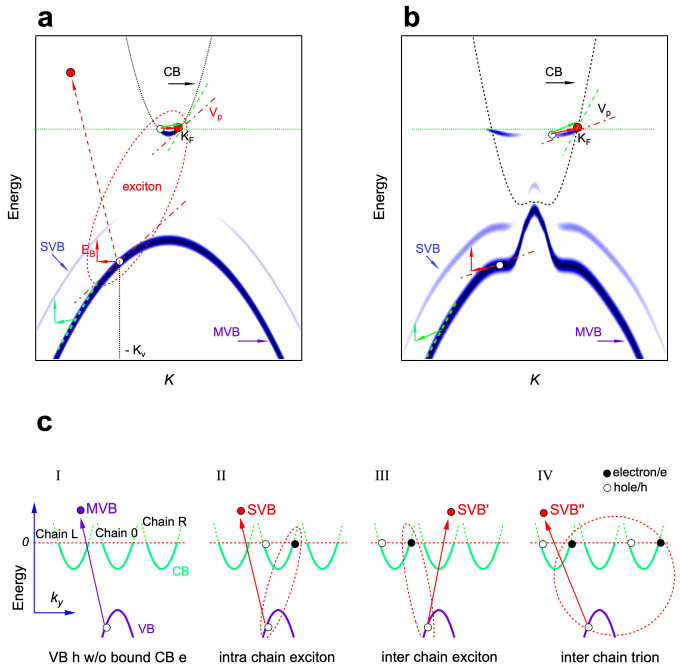


FIG. 4. Schematic of how mobile excitons show up in the form of SVBs in photoemission. **a** Toy model with parabolic VB and CB. The drawing shows excitonic excitations for total momenta $K > K^*$ where a VB hole with velocity $v_{\mathrm{h}} > v_{\mathrm{F}}$ binds to a CB electron above the Fermi level. The SVB is constructed graphically. Starting from a VB state, the partner state with equal group velocity (slope of the dispersion) in the CB is determined. The energy-momentum transfer from the left Fermi point to that state is combined with a vertical shift by the (momentum independent) binding energy to obtain a point on the excitonic side branch. **b** The same procedure applied to a more realistic model of $TaSe_3$. The simple parabolic Fermi sea is replaced by high intensity islands in the polaronic band, its diameter Δk playing the role of $2k_{\mathrm{F}}$ in **a**. The binding energy now depends on the curvature of the VB and the CB at the momenta involved in the exciton pair. The SVB construction results in an excitonic branch which is a nearly parallel translate of the simple hole dispersion, the MVB. **c** Proposed origin of the MVB and the various SVBs. The MVB **I** results from a single VB hole excitation. It costs less energy (at given momentum K) if it is accompanied by particle-hole excitations in the CB of the same or neighboring chains. The binding of the CB particle(s) with the VB hole results in various types of excitonic modes, namely intrachain exciton **II**, interchain excitons **III**, and possibly interchain trions **IV**.

[1] Nagaosa, N., *Quantum Field Theory in Strongly Correlated Electronic Systems*. Theoretical and Mathematical Physics. Springer Berlin Heidelberg, 1999.

[2] Giamarchi, T., and Press, O. U. *Quantum Physics in One Dimension*. International Series of Monogr. Clarendon Press, 2004.

[3] Frenkel, J. On the transformation of light into heat in solids. i. *Phys. Rev.* **37**, 17–44 (1931).

[4] Wannier, G. H. The structure of electronic excitation levels in insulating crystals. *Phys. Rev.* **52**, 191–197 (1937).

[5] Kasha, M. Relation between exciton bands and conduction bands in molecular lamellar systems. *Rev. Mod. Phys.* **31**, 162–169 (1959).

[6] Knox, R. S. *Introduction to Exciton Physics*. Springer US, Boston, MA, 1983, pp. 183–245.

[7] Combescot, M., and Shiau, S. *Excitons and Cooper Pairs: Two Composite Bosons in Many-body Physics*. Oxford graduate texts. Oxford University Press, 2016.

[8] Wang, G. et al. Colloquium: Excitons in atomically thin transition metal dichalcogenides. *Rev. Mod. Phys.* **90**, 021001 (2018).

[9] Hong, J., Senga, R., Pichler, T., and Suenaga, K. Probing exciton dispersions of freestanding monolayer WSe_2 by momentum-resolved electron energy-loss spectroscopy. *Phys. Rev. Lett.* **124**, 087401 (2020).

[10] Seki, K., Excitonic Bose-Einstein condensation in Ta_2NiSe_5 above room temperature. *Phys. Rev. B* **90**, 155116 (2014).

[11] Sugawara, K. et al. Unconventional charge-density-wave transition in monolayer $1T$-$TiSe_2$. *ACS Nano* **10**, 1341–1345 (2016).

[12] Srivastava, S. K., and Avasthi, B. N. Preparation, structure and properties of transition metal trichalcogenides. *Journal of Materials Science* **27**, 3693 (1992).

[13] Island, J. O. et al. Electronics and optoelectronics of quasi-1d layered transition metal trichalcogenides. *2D Materials* **4**, 022003 (2017).

[14] Sambongi, T. Superconductivity in one-dimensional $TaSe_3$. *Journal of the Physical Society of Japan* **42**, 1421–1422 (1977).

[15] Tsutsumi, K. Direct electron-diffraction evidence of charge-density-wave formation in $NbSe_3$. *Phys. Rev. Lett.* **39**, 1675–1676 (1977).

[16] Yamamoto, M. Superconducting properties of $TaSe_3$. *Journal of the Physical Society of Japan* **45**, 431–438 (1978).

[17] Haen, P., Lapierre, F., Monceau, P., Regueiro, M. N., and Richard, J. Low temperature phase transition in the chain-like compounds $NbSe_3$ and $TaSe_3$. *Solid State Communications* **26**, 725–730 (1978).

[18] Ekino, T., and Akimitsu, J. Electron tunneling study of $NbSe_3$. *Japanese Journal of Applied Physics* **26**, 625 (1987).

[19] Cava, R. J., Fleming, R. M., Dunn, R. G., and Rietman, E. A. Low-frequency dielectric response of the charge-density wave in orthorhombic $TaSe_3$. *Phys. Rev. B* **31**, 8325–8328 (1985).

[20] Nagata, S., Kutsuzawa, H., Ebisu, S., Yamamura, H., and Taniguchi, S. Superconductivity in the quasi-one-dimensional conductor $TaSe_3$. *Journal of Physics and Chemistry of Solids* **50**, 703–707 (1989).

[21] Nomura, A. et al. Emergence of a resistance anomaly by cu-doping in $TaSe_3$. *EPL (Europhysics Letters)* **119**, 17005 (2017).

[22] Nomura, A., Yamaya, K., Takayanagi, S., Ichimura, K., and Tanda, S. Effect of Cu doping on superconductivity in $TaSe_3$.: Relationship between superconductivity and induced charge density wave. *EPL (Europhysics Letters)* **124**, 67001 (2019).

[23] Yang, J. Observation of charge density wave transition in $TaSe_3$ mesowires. *Applied Physics Letters* **115**, 033102 (2019).

[24] Nie, S. et al. Topological phases in the $TaSe_3$ compound. *Phys. Rev. B* **98**, 125143 (2018).

[25] Chen, C. et al. Observation of topological electronic structure in quasi-1d superconductor $TaSe_3$. *Matter* **3**, 2055–2065 (2020).

[26] Lin, C. et al. Visualization of the strain-induced topological phase transition in a quasi-one-dimensional superconductor $TaSe_3$. *Nature Materials* **20**, 1093–1099 (2021).

[27] Lampert, M. A. Mobile and immobile effective-mass-particle complexes in nonmetallic solids. *Phys. Rev. Lett.* **1**, 450–453 (1958).

[28] Kheng, K. et al. Observation of negatively charged excitons x^- in semiconductor quantum wells. *Phys. Rev. Lett.* **71**, 1752–1755 (1993).

[29] Matsunaga, R., Matsuda, K., and Kanemitsu, Y. Observation of charged excitons in hole-doped carbon nanotubes using photoluminescence and absorption spectroscopy. *Phys. Rev.*

Lett. **106**, 037404 (2011).

[30] Efimkin, D. K., and MacDonald, A. H. Many-body theory of trion absorption features in two-dimensional semiconductors. *Phys. Rev. B* **95**, 035417 (2017).

[31] Rivera, P., Schaibley, J. R., Jones, A. M., Ross, J. S., Wu, S., Aivazian, G., Klement, P., Seyler, K., Clark, G., Ghimire, N. J., and et al. Observation of long-lived interlayer excitons in monolayer mose2–wse2 heterostructures. *Nature Communications* **6**, 1 (2015).

[32] Wilson, N. R. Determination of band offsets, hybridization, and exciton binding in 2d semiconductor heterostructures. *Science Advances* **3**, 2 (2017).

Methods

Crystal synthesis and structure. Single crystals of $TaSe_3$ were synthesized using evenly-ground stoichiometric elemental Ta ($\sim$ 325 mesh, Beamtown Chemical, $\geq$ 99.9%) and Se ($\sim$ 200 mesh, Beamtown Chemical, $\geq$ 99.999%) with a total mass of $\sim$ 300mg were pressed into a pellet and placed in an evacuated quartz tube mixed with $\sim$ 10mg of I_2 as the vapor transport medium. The tube was put into a tube furnace and heated up to 700°C on the sample side while the other side of the tube, while in the furnace, was open to the external environment so as to generate a temperature gradient. After holding the sample at 700°C for five days, the furnace was shut down and cooled to room temperature. Needle-like crystals $TaSe_3$ can be found at the cooler side of the quartz tube. The trichalcogenide $TaSe_3$ is a representative of the family of crystals XT_3 where X belongs to either the group IVB (Ti, Zr, Hf) or the group VB (Nb, Ta), and T is a chalcogen from the group VIA (S, Se, Te). The crystalline structure of $TaSe_3$ is monoclinic with the space group $P2_1/m$ (SG11). The selenium atoms are located at the vertices of triangular prisms with three faces parallel to the *b*-axis and a tantalum atom at their center. These prisms are covalently stacked along the *b*-axis and form parallel one-dimensional (1D) chains. The unit cell viewed along the *b*-axis contains four triangular prisms, with covalent bonds along the (101) direction. Thus, the natural cleavage plane is the $(10\bar{1})$ surface.

ARPES experiments. ARPES measurements were performed at the SIS-ULTRA beamline and at the ADRESS-ARPES beamline of the Swiss Light Source, Paul Scherrer Institute, and at the beamline UE112 PGM-2b-1^3 at BESSY (Berlin Electron Storage Ring Society for Synchrotron Radiation) Synchrotron. The energy and angular resolutions were set to $5 - 30\,\mathrm{meV}$ and 0.1°, respectively. The samples for ARPES measurements were

cleaved in situ and measured mainly in a temperature range between 15K and 25K in a vacuum exceeding 8×10^{-11}Torr.

First-Principles calculations. The first-principles calculations were performed within the framework of the full-potential linearized augmented plane-wave method implemented in the WIEN2K simulation package. A modified Becke-Johnson exchange potential together with the local-density approximation for the correlation potential was used to obtain accurate band structures. Spin-orbit coupling (SOC) was included as a second, self-consistent variational step. The radii of the muffin-tin sphere R_{MT} were 2.5 Bohr for Ta and 2.38 Bohr for Se. The $\boldsymbol{k}$-point sampling grid of the BBZ in the self-consistent process was $7 \times 19 \times 6$. The truncation of the modulus of the reciprocal lattice vector K_{max}, which was used for the expansion of the wave functions in the interstitial region, was set to $R_{\mathrm{MT}}\, K_{\mathrm{max}}$=7. The geometry optimization including SOC was carried out within the framework of the projector augmented-wave pseudopotential method implemented in the Vienna Ab initio Simulation Package. The ionic positions were relaxed until the force on each ion was less than $0.005\,\mathrm{eV/\AA}$.

Data Availability. The data that supports the findings of this study is available in the MARVEL public repository (MARVEL Materials Cloud Archive: https://archive.materialscloud.org) with same title of this paper.